Human ribosome interactions reframe neomycin toxicity

Meng Wu[1,#], Lingfan Zhu[1,#], Xinyi Zhang[1,#], Changfeng Jia[1,#], Keqin Wu[1,#], Chuansen Yi[1], Shuangli Sun[1], Zhe Zhang[1], Lei Guo[2], Xuben Hou[3,*], Alexey Amunts[4,5,*], Wenfei Li[1,2,*]

[1] School of Basic Medical Sciences, Cheeloo College of Medicine, Shandong University, Jinan, Shandong, China.

[2] Children's Hospital Affiliated to Shandong University, Jinan, Shandong, China

[3] Department of Medicinal Chemistry, Shandong Key Laboratory of Druggability Optimization and Evaluation for Lead Compounds, School of Pharmaceutical Sciences, Cheeloo College of Medicine, Shandong University, Jinan, Shandong, China.

[4] University of Münster, Schlossplatz 8, 48143 Münster, Germany

[5] Department of Structural Biochemistry, Max Planck Institute of Molecular Physiology, Otto-Hahn-Str. 11, 44227 Dortmund, Germany

[#] Equal contribution

[*] Correspondence to: wenfeili@sdu.edu.cn; alexey.amunts@gmail.com

Abstract

Aminoglycosides like neomycin are widely used but clinically limited due to toxicity, traditionally attributed to mitoribosome inhibition. Here, we demonstrate that this assumption requires re-evaluation by comparing neomycin's interactions with human ribosomes *in vitro* and in cells. While cryo-EM and biochemical assays reveal strong *in vitro* binding to both mitoribosomes and cytosolic ribosomes, especially at conserved regions such as the helix 44 (h44) decoding center despite sequence divergence, and H69. Cellular analyses show minimal impact on global translation, reduced occupancy on cytosolic ribosomes, and a complete absence of neomycin on mitoribosomes. These discrepancies suggest limited mitochondrial permeability rather than direct mitoribosome inhibition underlies neomycin's toxicity. Our findings redefine the mechanistic basis of aminoglycosides side effects and call for a reassessment of their cellular targets.

Introduction

Precise control of protein synthesis is fundamental to cellular life, and its disruption is a common target for antibiotics[1–4]. Although aminoglycosides are highly effective against bacteria, their systemic clinical use is constrained by significant oto- and nephrotoxicity in patients[5,6]. While selectivity of aminoglycosides for bacterial ribosomes is often attributed to structural variations within h44 decoding site compared to their eukaryotic counterparts[7,8], the structural similarity between bacterial and mitochondrial translation apparatus suggests a potential for off-target effects may underlie the observed human toxicities[9–15]. Aminoglycosides have been reported to interact with eukaryotic ribosomes, influencing translation fidelity or inducing premature termination codon readthrough[16–20]. Derivatives of aminoglycosides could further enhance specificity to eukaryotic ribosome for therapeutic purposes, such as leishmania targeting[21] or nonsense mutation suppression for genetic diseases[22].

Neomycin is a 4,5-linked aminoglycoside antibiotic[16,23] that inhibits bacterial translation primarily by binding to the decoding A site[24,25]. This involves binding to h44 of the small subunit (SSU) and H69 of the large subunit (LSU), thereby causing codon misreading and translation inhibition[3,24,26–28]. Molecular dynamics simulations of the decoding site showed that the catalytic activity also depends on rRNA A-site dynamics[29]. Despite the assumption that mitochondrial translation is the primary site of aminoglycoside toxicity, neomycin has also been shown to disrupt mitochondrial lipid metabolism, and promote pathological interactions with lipid droplets, leading to oxidative stress and impaired fatty acid utilization[30]. Thus, the understanding of neomycin's impact for guiding the development of safer therapeutic strategies warrants critical re-evaluation. A detailed investigation of neomycin's interaction with both human mitochondrial and cytosolic ribosomes is crucial for a complete picture of its cellular impact and for guiding the development of safer therapeutic strategies.

Previous studies successfully used addition of antibiotics streptomycin[31] and quinupristin/dalfopristin[32] directly to the cell culture to define their structures in the mitoribosome-bound form. In this study, we systematically investigate neomycin's action on mitoribosomes and cytosolic ribosomes from HEK (human embryonic kidney) 293-

60 derived cells. We determined the cryo-EM structures of human mitoribosomes and
61 cytosolic ribosomes bound to neomycin *in vitro*, then analyzed native ribosomes isolated
62 from drug-treated cells to assess neomycin's occupancy *in vivo.* Our results reveal
63 striking discrepancies between *in vitro* and *in vivo* drug behavior, including limited
64 engagement and selective loss of binding at key functional sites, such as h44, in the
65 cellular environment. These findings challenge the conventional views of neomycin's
66 mitochondrial toxicity and indicate that additional factors, including cellular bioavailability
67 barriers, redox-dependent binding plasticity, and ribosomal dynamics should be taken
68 into account when considering therapeutic strategies.

69

70 **Results**

71 **Distinct neomycin-binding landscape on human mitoribosome**

72 To investigate the molecular basis of neomycin's interaction with human mitoribosomes,
73 we performed cryo-EM on mitoribosomes rapidly isolated from HEK293F cells[33] and
74 incubated with 50 μM neomycin. This yielded six maps with average resolutions ranging
75 from 2.9−3.3 Å. These states were designated as "non-rotated A/A-P/P", "non-rotated
76 A/A-P/P-E/E", "partially rotated A/A-P/P-E/E", "partially rotated hybrid A/P-P/E", "rotated
77 empty", "rotated hybrid A/P-P/E" (**Supplementary Fig. 1, Supplementary Table 1**). The
78 map quality allowed us to consistently identify cofactors, including polyamines and Fe-S
79 clusters, associated with rRNA and proteins, in agreement with previous reports[15,31]
80 (**Supplementary Fig. 1c-d**). Neomycin is composed of four linked monosaccharide rings
81 (I-IV), including a central 2-deoxystreptamine (ring II) and three amino-modified sugars
82 (**Fig. 1a**). Across the six states, we identified nine distinct densities corresponding to
83 neomycin molecules: three on the mitochondrial small ribosomal subunit (mtSSU) (Neo1-
84 3) and six on the mitochondrial large ribosomal subunit (mtLSU) (Neo4-9) (**Fig. 1b**,
85 **Supplementary Table 2**).

86 Specifically, Neo1 displayed well-defined density for all four rings (I-IV) and bound to h44
87 adjacent to the A-tRNA binding site within the decoding center (**Fig. 1c, Supplementary**
88 **Fig. 2, Supplementary Fig. 3a and d**). This binding effectively blocks proper pairing of

89 tRNA with mRNA, consistent with observations in bacterial ribosomes[24,25]
90 (**Supplementary Fig. 3a**). Neo1 establishes potential hydrogen bonds with several
91 nucleotides from the mtSSU including G1489, U1490, C1491, A1555, A1557, A1558,
92 G1559 and U1560 (**Fig. 1c, Supplementary Fig. 2d**). Notably, ring I of Neo1 forms stable
93 π-π stacking with the nucleobase C1556 (**Fig. 1c, Supplementary Fig. 2d**). Furthermore,
94 two conserved nucleotides, A1447 and A1558 (equivalent to A1492/A1493 in bacteria),
95 are observed to flip out of h44 (**Fig. 1c**), a characteristic of sampling the codon-anticodon
96 interaction that facilitates near cognate tRNA incorporation of incorrect amino acid during
97 protein synthesis[34–36].

98 The Neo2 molecule, situated in a pocket formed by h1 and h44, displayed well-identified
99 density for all four rings (**Fig. 1d, Supplementary Fig. 3c-d**). It establishes potential
100 hydrogen bonds with the nucleobase of C1481 and sugar-phosphate backbone of U656,
101 G657, G658 and G899 from the mtSSU (**Fig. 1d**). Similarly, the Neo3 molecule binds to
102 h28 near the P-tRNA, stabilized by hydrogen bonds with nucleotides from the mtSSU
103 (specifically, the phosphate group of G1469 and A1470; and the nucleobases from G1472,
104 C1473, G1474, G1178, U1180 and C1182) (**Fig. 1e, Supplementary Fig. 3c-d**). Neo4
105 binds to the terminal hairpin of H69 with a relatively less well-identified density (**Fig. 1f,**
106 **Supplementary Fig. 3d)**. It is stabilized by nucleotides from both the mtSSU (G1079
107 U1081 and G1582) and mtLSU (C2583 and U2586) (**Fig. 1f, Supplementary Fig. 2e,**
108 **Supplementary Fig. 3b-c**). H69 is recognized as another critical binding pocket for
109 aminoglycosides. Consistent with previous bacterial structural data[24,25], Neo1 and Neo4
110 represent conserved neomycin binding sites in human mitoribosomes, located within the
111 h44 and H69 regions, respectively (**Supplementary Fig. 3a-b**).

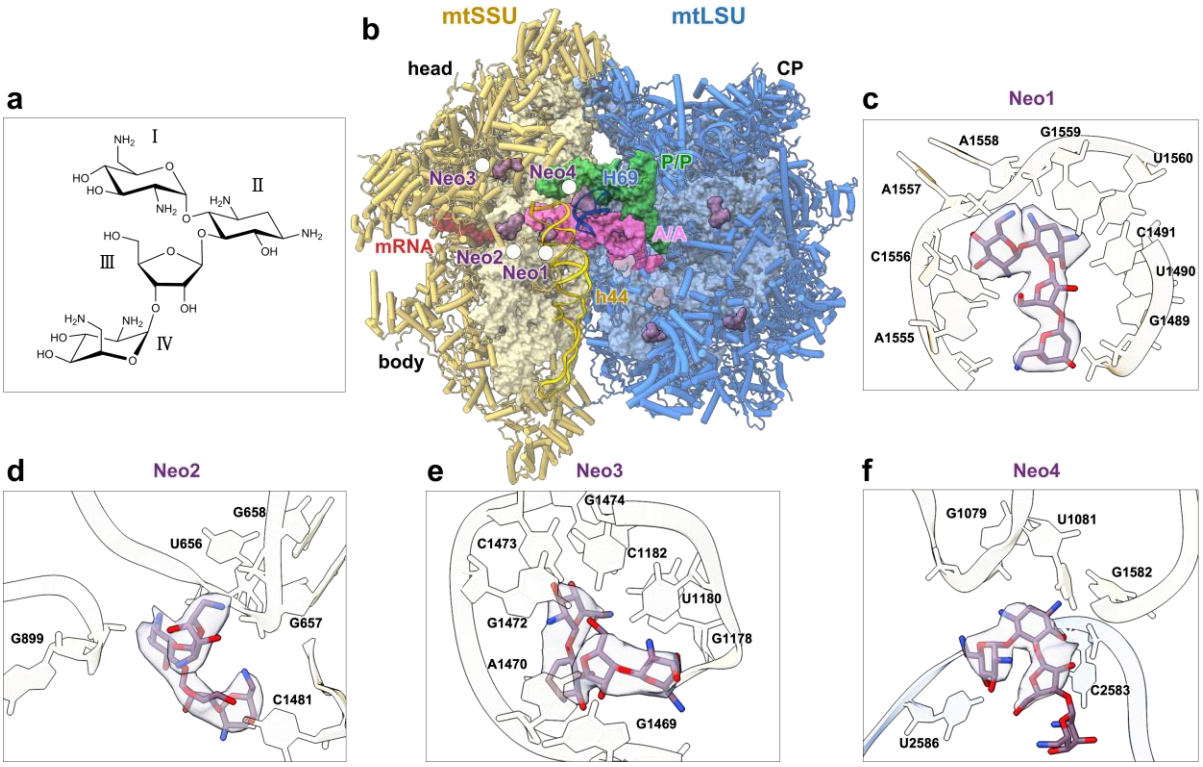

Fig. 1| Structural analysis of neomycin binding to mitoribosome *in vitro*. a Chemical structure of neomycin. **b** Overall structure of the neomycin-bound mitoribosome in non-rotated state comprising the mtSSU (yellow), mtLSU (blue), mRNA (red), A-site tRNA (magenta) and P-site tRNA (green). rRNA helices h44 and H69 are shown in cartoon in gold and blue, respectively. **c** Close-up view of Neo1 occupying the conserved pocket formed by h44. **d** Close-up view of Neo2 binding pocket formed by residues from h1 and h44. **e** Close-up view of Neo3 binding pocket in h28. **f** Close-up view of Neo4 binding pocket formed by H69 and stabilized by nucleotides from both H69 and the mtSSU. Key interacting nucleotides are represented as sticks (oxygen in red, nitrogen in blue).

The engagement of neomycin, particularly at h44 and H69, was found to be dependent on the rotational state of the mitoribosome (**Supplementary Table 2**). Specifically, Neo1 binds to h44, exhibited well-defined density for all four of its rings across various non-rotated and partially rotated states (**Supplementary Table 2, Supplementary Fig. 3d**). However, it was notably absent in the functional rotated state containing A/P and P/E tRNAs (**Supplementary Table 2**). This suggests that neomycin binding to h44

129 preferentially stabilizes non-rotated or partially rotated conformations, thereby preventing
130 the mitoribosome from fully entering the functional rotated state. This observation aligns
131 with findings in bacterial systems, where neomycin binding to h44 is known to restrict
132 subunit rotation and maintain a non-rotated state, providing a structural basis for its
133 inhibitory mechanism[24,27].

134 For H69, discernible densities for rings I to III of neomycin were observed in both rotated
135 and non-rotated states only when tRNAs occupied the A and P sites (**Fig. 1f,**
136 **Supplementary Table 2, Supplementary Fig. 3d**). Intriguingly, H69 binding was absent
137 in partially rotated states (**Supplementary Table 2**). This indicates that H69 binding is
138 contingent upon specific tRNA occupancy and ribosomal conformation, favoring either
139 the non-rotated or fully rotated states with engaged tRNAs. Collectively, this
140 conformational state-dependent binding of neomycin to both h44 and H69 on the
141 mitoribosome suggests a dynamic interplay between drug association and the ribosome's
142 structural landscape, paralleling similar mechanisms observed in bacterial ribosomes.

143

144 **Structural analysis reveals canonical and novel neomycin-binding sites on the**
145 **human cytosolic ribosome**

146 To understand the impact of neomycin on human cellular translation and its potential
147 toxicity, we assessed its interaction with human cytosolic ribosomes (**Supplementary Fig.**
148 **4, Supplementary Table 3**). While previous studies have indicated sequence differences
149 in the critical h44 region of human ribosomes compared to their bacterial counterparts
150 (**Supplementary Fig. 2a-c**), potentially affecting aminoglycoside binding[3,24,26–28], our *in*
151 *vitro* translation (IVT) assays revealed that neomycin significantly inhibits cytosolic
152 ribosomes activity, with a half-maximal inhibitory concentration (IC_{50}) of approximately 50
153 μM (**Fig. 2a**). This finding suggests that neomycin can effectively target human cytosolic
154 ribosomes and inhibit its translation.

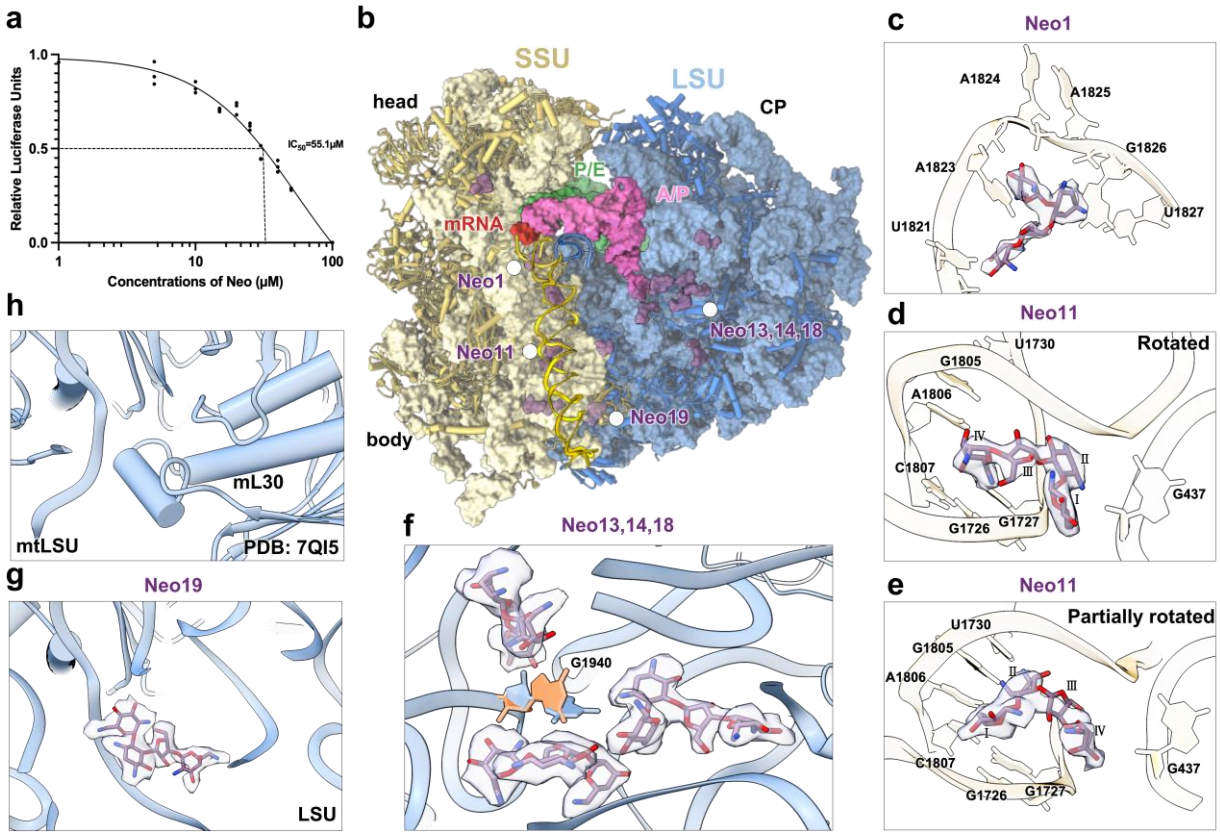

Fig. 2| Structural analysis of neomycin binding to cytosolic ribosomes *in vitro*. a Luciferase reporter assays of cytosolic ribosomes in response to neomycin at different concentrations of 1, 5, 10, 15, 20, 25, 30, 40, 50 and 100 μM (data are presented as mean ± s.d., n = 3 independent experiments). **b** Overall structure of neomycin-bound cytosolic ribosomes in rotated state comprising the SSU (yellow), LSU (blue), mRNA (red), A/P-site tRNA (magenta) and P/E-site tRNA (green). rRNA helices h44 and H69 are shown in cartoon in gold and blue, respectively. **c** Close-up view of Neo1 bound to h44. **d** Close-up view of Neo11 bound to a novel pocket within h44 in the rotated state. **e** A different conformation of Neo11 bound to in the partially rotated state. **f** A novel pocket accommodating three neomycin molecules (Neo13, Neo14, and Neo18), with G1940 adopting a unique conformation upon neomycin binding (orange: pre-binding conformation, blue: post-binding conformation). **g** Close-up view of Neo19 bound to a pocket formed by H53 and H54 from the LSU. **h** Comparison showing that in the mitoribosome, the Neo19 site is preoccupied by mitochondrial protein mL30 (PDB: 7QI5[15]).

172 To further elucidate the molecular mechanism of this inhibition and the specific binding
173 modes of neomycin on the cytosolic ribosome, we subsequently performed cryo-EM
174 analysis of cytosolic ribosome complexes incubated with 50 μM neomycin (**Fig. 2**,
175 **Supplementary Fig. 4, Supplementary Table 3**). Our single-particle analysis yielded
176 structures of ribosomes in three distinct translational states: a non-rotated state with P/P
177 and E/E-site tRNA; a partially rotated state with eEF2, SERBP1 and E/E-site tRNA; and
178 a rotated state with A/P and P/E-site tRNA (**Supplementary Fig. 4a**). Across these maps,
179 we identified neomycin molecules bound at 17 distinct pockets: three on the small
180 ribosomal subunit (SSU) (Neo1, Neo10 and Neo11) and fourteen on the large ribosomal
181 subunit (LSU) (Neo12-Neo25) (**Fig. 2b, Supplementary Table 4, Supplementary Fig.**
182 **5**). Notably, the majority of these binding pockets were consistently occupied by neomycin
183 across the different ribosomal states (**Supplementary Table 4**).

184 A well-established mechanism for aminoglycoside action in bacteria involves binding to
185 the decoding center, primarily formed by h44 of the small subunit[3,24,26–28]. We observed
186 analogous binding in the human cytosolic ribosome despite sequence differences (**Fig. 2,**
187 **Supplementary Fig. 2a-c**). Our structures of the neomycin-bound human cytosolic
188 ribosome revealed Neo1 at the universally conserved aminoglycoside binding pocket
189 within h44 (**Fig. 2b-c, Supplementary Table 4, Supplementary Fig. 5a-c and h**). While
190 the overall binding mode is conserved, superimposition of human and bacterial h44
191 structures indicated slight conformational changes and subtle differences in the precise
192 neomycin binding pose (**Supplementary Fig. 5a-c**). Neo1 interacts with U1821-U1827
193 of h44, with A1824 and A1825 (equivalent to A1492/A1493 in bacteria) flipped out from
194 the helix, consistent with observations in bacteria and mitoribosomes (**Fig. 1c, Fig. 2c**).

195 Intriguingly, we also identified a second neomycin molecule (Neo11) bound to a novel,
196 distinct pocket located centrally on h44, away from the canonical A-site tRNA binding
197 region (**Fig. 2d-e, Supplementary Fig. 5h**). The conformation of Neo11 within this pocket
198 exhibited significant differences between the partially rotated and rotated states (**Fig. 2d-**
199 **e**). Specifically, in the rotated ribosome, ring I of Neo11 directly interacts with G437 from
200 the SSU via a hydrogen bond, while ring IV forms hydrogen bonds with h44 residues,
201 including G1726, G1727 and A1806 (**Fig. 2d**). In contrast, in the partially rotated state
202 (characterized by an approximate 5° rotation of the SSU relative to the one from the

203 rotated state), this pocket undergoes a spatial displacement of approximately 3 Å.
204 Meanwhile, Neo11 undergoes a 180° flip with its ring I approaching the A1806 direction
205 (**Fig. 2e**). This conformational rearrangement leads to entirely distinct interactions
206 between Neo11 and h44: ring I forms a hydrogen bond with C1807, ring II interacts with
207 U1730 and G1805 (proximal of A1806), and ring IV engages with the phosphate group of
208 G1726 and G1727 (**Fig. 2e, Supplementary Fig. 5h**). These latter interactions, where
209 nucleobases stabilize neomycin, occur specifically in the rotated state. These dynamic
210 binding characteristics suggest a potential link between the novel Neo11 binding site and
211 ribosome dynamics. Notably, unlike in bacterial ribosomes and mitoribosomes where H69
212 is a conserved aminoglycoside pocket, no neomycin binding was observed to H69 of the
213 human cytosolic ribosome, likely due to sequence differences in human H69 causing a
214 relatively smaller pocket and potential steric clash (**Supplementary Fig. 5d**).

215 Beyond these h44-proximal sites, we identified a large, previously uncharacterized pocket
216 formed by helices H89 and H72 of the LSU rRNA and a conserved rRNA loop (C1928-
217 C2053) (**Fig. 2f**). This pocket simultaneously accommodates three neomycin molecules
218 (Neo13, Neo14, and Neo18) (**Fig. 2f, Supplementary Fig. 5h**). Upon neomycin binding
219 within this pocket, we observed a distinct conformational change in nucleotide G1940
220 (**Fig. 2f**). This specific conformational alteration of G1940 was consistently present across
221 all structural classes of neomycin-bound ribosomes. Analyzing the identified binding
222 pockets revealed significant differences compared to those observed in mitoribosomes,
223 with the exception of the universally conserved Neo1 site (**Supplementary Tables 2 and**
224 **4**). Several neomycin-binding pockets appeared to be specific to the human cytosolic
225 ribosome, occupying regions that correspond to different ribosomal proteins in the
226 bacterial ribosome or mitoribosome (**Fig. 2g-h, Supplementary Fig. 5e-g**). For example,
227 Neo19 binds to a pocket formed by LSU nucleotides, a pocket that is absent in
228 mitoribosomes as it is occupied by the mL30 protein (**Fig. 2g-h**). These differences
229 highlight the distinct structural landscapes of various ribosomes. Collectively, these
230 multiple binding interactions, particularly at the h44 decoding center, provide a structural
231 rationale for the neomycin-induced inhibition of cytosolic translation observed in our IVT
232 assays (**Fig. 2**).

233

Absence of neomycin binding to mitoribosomes in cells

While our cryo-EM data analysis revealed multiple binding of neomycin to both mitoribosomes and cytosolic ribosomes *in vitro* (**Figs. 1 and 2**), its effects on cellular translation were mild. Cell viability assays (CCK8) indicated limited cytotoxicity upon short-term neomycin exposure with an IC_{50} of approximately 1.2 mM after prolonged (72 h) treatment (**Fig. 3a**). Consistent with this, L-azidohomoalanine (L-AHA) labeling assay (a method for detecting newly synthesized nascent chains)[37–39] showed no significant change of global mitochondrial translation (**Fig. 3b**).

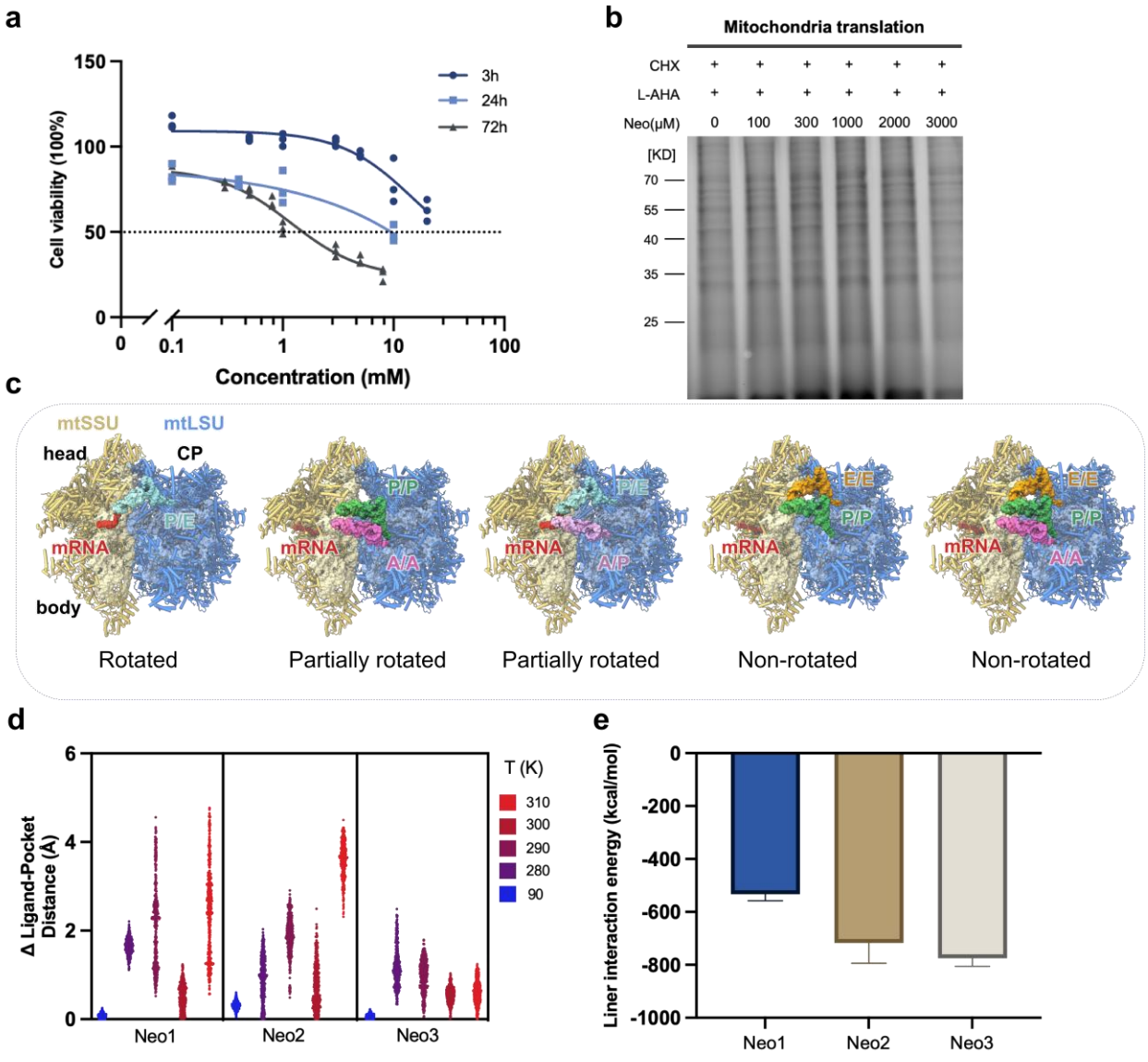

244 **Fig. 3| *In vivo* effects and structural dynamics of neomycin on human**
245 **mitoribosomes**. **a** Cell viability of HEK293T cells measured by the CCK-8 assay after
246 treatment with increasing concentrations of neomycin for 3 h, 24 h, and 72 h, respectively
247 (data are presented as mean ± s.d., n = 3 independent experiments). **b** *De novo*
248 mitochondrial nascent protein synthesis measured via L-AHA labeling. **c** Overall cryo-EM
249 structure of native mitoribosome with different tRNAs and cofactors. Coloring is consistent
250 with previous figures. **d** MD simulations depicting the temperature-dependent binding
251 stability of neomycin molecules (Neo1, Neo2, and Neo3) within the mtSSU, illustrating
252 the relative movement of the neomycin molecules within their binding pocket. The
253 changes in distance between the ligand mass center and the binding pocket mass center
254 (defined as the centroid of residues within 3 Å of the ligand in initial cryo-EM structure)
255 during molecular dynamics simulations at temperatures ranging from 90 K to 310 K. **e**
256 Calculated linear interaction energy for neomycin within the mtSSU.
257

258 To investigate this discrepancy between *in vitro* potency and *in vivo* cellular effects, we
259 conducted comprehensive structural, biochemical and computational analysis of the
260 native ribosome (**Supplementary Figs. 6-10**). We isolated the native translation
261 complexes from the kidney-derived HEK293F cells treated with 1 mM neomycin. This
262 concentration, while higher than typical plasma levels (up to ~0.13 mM), is clinically
263 relevant as neomycin accumulates to millimolar concentrations in the kidney—a primary
264 site of its toxicity[40,41]. As previously shown[31,42,43] this approach implies that the
265 antimicrobial would have to be imported into mitochondria, preserving more native states.
266 Mitoribosomes were then isolated and subjected to a cryo-EM analysis (**Supplementary**
267 **Fig. 6, Supplementary Table 5**).

268 The cryo-EM analysis of mitoribosomes from treated cells yielded six distinct translational
269 states characterized by varying SSU rotations and associated translation factors (**Fig. 3c,**
270 **Supplementary Fig. 6**). Consistent with our biochemical data showing limited cellular
271 toxicity and effect on mitochondrial translation upon neomycin treatment (**Fig. 3a-b**), our
272 structural analysis revealed a striking absence of bound neomycin molecules on human
273 mitoribosomes isolated from these treated cells (**Fig. 3c, Supplementary Table 2**). This
274 indicates that under the cellular conditions, neomycin does not stably associate with or

275 significantly inhibit human mitoribosomes *in vivo*.

276 At physiological temperatures, biomolecules can access a broader range of
277 conformations, and the rates of conformational switching are generally faster than at
278 lower temperatures[44]. Although rapid cooling during cryo-EM sample preparation can
279 kinetically trap molecules in states representative of the room-temperature ensemble[3,44].
280 It remains crucial to assess if the binding pocket for neomycin adopts a non-binding-
281 competent conformation specifically at physiological cellular temperatures *in vivo*. To
282 investigate this, we performed all-atom explicit-solvent molecular dynamics (MD)
283 simulations of the mtSSU with bound neomycin, focusing on the decoding center (**Fig.
284 3d-e, Supplementary Fig. 9**). Molecular dynamics (MD) simulations were initiated from
285 the cryo-EM structure and performed across a range of temperatures up to physiological
286 conditions. For each temperature, five independent replicates were conducted,
287 accumulating a total simulation time of 0.5 μs. As anticipated, the fluctuation of the
288 antibiotic's binding pockets and its atomic positions, quantified by root mean square
289 deviation (RMSD) analysis, increased with rising temperature (**Supplementary Fig. 9a-
290 c**). Despite these thermal fluctuations, the neomycin molecules remained stably
291 associated with their binding sites within the mitoribosome (**Fig. 3d**). The consistent
292 association of neomycin with its mitoribosomal binding sites even at physiological
293 temperatures effectively rules out temperature-driven conformational changes as the sole
294 reason for its observed absence *in vitro*. Furthermore, comparative analysis of the MD
295 trajectories revealed enhanced binding stability of neomycin at the Neo1 site relative to
296 Neo2 and Neo3, evidenced by lower ligand RMSD values and reduced calculated linear
297 interaction energy (**Fig. 3e**).

298

299 **Reduced engagement of neomycin with human cytosolic ribosomes *in vivo***

300 Despite strong *in vitro* inhibition of cytosolic ribosomes and observed binding to the key
301 h44 site in *in vitro* incubated structures (**Fig. 2**), neomycin treatment did not markedly
302 inhibit nanoluciferase expression in cells, even at high concentrations (**Fig. 4a,
303 Supplementary Fig. 8a and c**). This suggests a limited overall effect on cellular
304 translation. Although L-AHA labeling assay showed no significant change of global

305 cytosolic translation, we did observe an increase in stop codon readthrough in a reporter
306 cell line upon neomycin treatment (**Fig. 4b-c, Supplementary Fig. 8b**). This suggests
307 that neomycin can influence cytosolic translation fidelity, even with minimal overall
308 inhibition. To further understand neomycin's cellular effect on cytosolic translation, we
309 isolated cytosolic ribosomes from the same batch of neomycin-treated cells used for
310 mitoribosome analysis. Our analysis revealed ribosomes in four different states, with the
311 rotated state being the most prevalent (**Supplementary Fig. 7, Supplementary Table**
312 **5**). We detected 15 neomycin molecules bound to the ribosomes, occupying some of the
313 same pockets identified in our *in vitro* incubation experiments (**Supplementary Table 4**).
314 Notably, densities for some sites such as Neo21 and Neo19 were diminished or absent
315 in the cellular samples compared to the *in vitro* incubated ribosomes (**Supplementary**
316 **Table 4**). Strikingly, the Neo1 site within the canonical h44 decoding center, a key binding
317 site *in vitro*, was completely devoid of neomycin in the cellular dataset (**Supplementary**
318 **Table 4, Fig. 4d**). This absence occurred despite no significant conformational changes
319 in the h44 pocket or novel post-translational modifications in the decoding center
320 (**Supplementary Fig. 8e**). We performed temperature-dependent MD simulations on the
321 SSU was conducted for the SSU with its bound neomycin molecules, including Neo1.
322 Although the neomycin molecules and their binding pocket displayed conformational
323 change with increasing temperatures (**Supplementary Fig 9d-f**), their binding relative to
324 their pockets remained stable with minor RMSD during simulations (**Fig. 4e**), excluding
325 temperature-driven conformational changes as the sole cause for its *in vitro* absence.
326 Additionally, neomycin binding at Neo1 site exhibited significantly stronger affinity than at
327 Neo10 or Neo11 from the SSU, evidenced by much lower interaction energies (**Fig. 4f**),
328 indicating that the lack of h44 bound neomycin is not due to weak binding affinity.

329 Our *in vivo* structural findings, particularly the reduced occupancy on cytosolic ribosomes
330 (**Supplementary Table 4**), suggest that the cellular environment critically modulates
331 neomycin's interactions, contrasting with direct incubation experiments. Given that prior
332 research has highlighted the protective effect of GSH against neomycin toxicity[45,46], we
333 examined the role of the cellular redox state. To test this, we performed *in vitro* and *in*
334 *vivo* translation assays using both oxidizing and reducing agents, but found no significant
335 change in neomycin's inhibitory action (**Fig. 4g-h, Supplementary Fig. 8d**). This

suggests that the redox state is not the primary factor responsible for the restricted binding at the h44 site or the observed *in vivo* translational effects (**Supplementary Table 4**). Moreover, at higher concentrations (3 mM) and prolonged exposure, neomycin binding became restricted to only two pockets (**Supplementary Tables 4-5, Supplementary Fig. 10**), suggesting that cellular mechanisms, such as drug efflux, may actively limit neomycin's interaction with its targets.

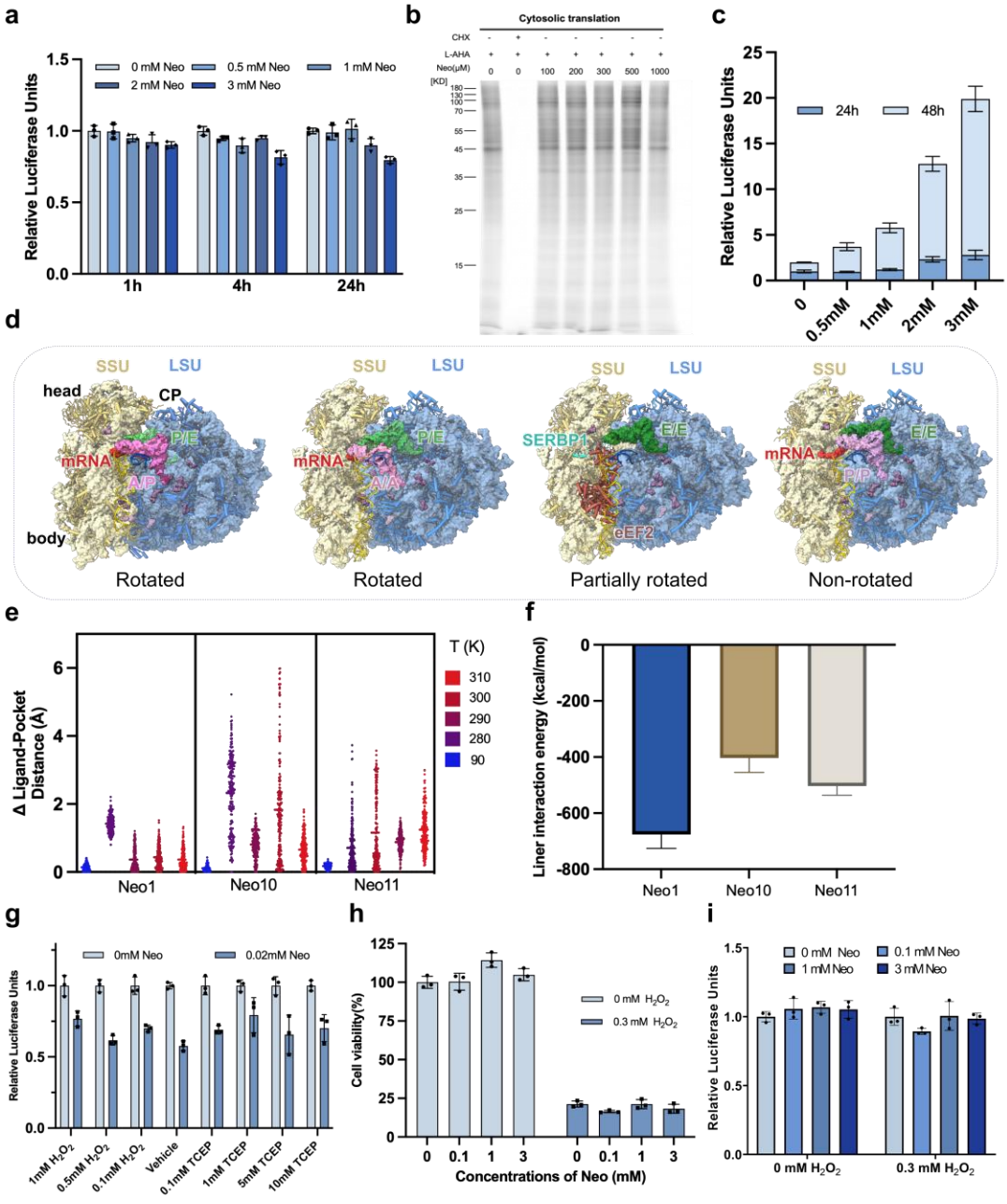

343 **Fig. 4| *In vivo* effects and structural analysis of neomycin with human cytosolic**
344 **ribosomes. a** *In vivo* translation assays using the NLuc cell line at various time points
345 following treatment with different concentrations of neomycin (data are presented as
346 mean ± s.d., n = 3 independent experiments). **b** *De novo* nascent protein synthesis
347 measured via L-AHA labeling. **c** Quantification of cystic fibrosis transmembrane
348 conductance regulator (CFTR) nonsense allele readthrough in cultured HEK293T cells
349 treated with increasing concentrations of neomycin for 24 h and 48 h (data are presented
350 as mean ± s.d., n = 3 independent experiments). **d** Overall cryo-EM structure of native
351 cytosolic ribosomes with different tRNAs and cofactors. Coloring is consistent with
352 previous figures. **e** MD simulations depicting the temperature-dependent binding stability
353 of neomycin molecules (Neo1, Neo10, and Neo11) within the SSU, illustrating the relative
354 movement of the neomycin molecules within their binding pocket. The changes in
355 distance between the ligand's center of mass and the binding pocket's center of mass
356 (defined as the centroid of residues within 3 Å of the ligand in initial cryo-EM structure)
357 during molecular dynamics simulations at temperatures ranging from 90 K to 310 K. **f**
358 Calculated linear interaction energy for neomycin within the SSU. **g** *In vitro* translation
359 assays with luciferase reporters were performed in the presence of 0.02 mM neomycin
360 under varying redox conditions. The redox conditions are mimicked by adding different
361 concentrations of H_2O_2 and TCEP. The vehicle group presents the condition with no
362 additional redox agents (data are presented as mean ± s.d., n = 3 independent
363 experiments). **h** Cell viability of HEK293T cells measured by the CCK-8 assay after
364 treatment with increasing concentrations of neomycin in the presence or absence of H_2O_2
365 (data are presented as mean ± s.d., n = 3 independent experiments). **i** *In vivo* translation
366 assays with luciferase reporters in response to different concentrations of neomycin in a
367 0.3 mM H_2O_2 environment (data are presented as mean ± s.d., n = 3 independent
368 experiments).
369

370 **Discussion**

371 This study provides insights into neomycin's interaction with human ribosomes by
372 uncovering the differences between its *in vitro* binding properties and in-cell behavior. We
373 show that neomycin's activity is modulated by the cellular environment, which can

374 diminish or prevent its engagement with key ribosomal targets. Our findings highlight a
375 clear divergence between *in vitro* and *in vivo* neomycin-ribosome interactions. *In vitro*,
376 neomycin robustly binds conserved sites on both mitoribosomes and cytosolic ribosomes,
377 including the bacterial-like decoding center at h44 (**Figs. 1-2, Supplementary Tables 2**
378 **and 4**). Crucially, however, in cells neomycin fails to occupy these sites, most notably
379 h44 in cytosolic ribosomes, and is undetectable on mitoribosomes (**Figs. 3-4**,
380 **Supplementary Table 2**). These observations correlate with minimal inhibition of global
381 translation, suggesting intracellular factors, such as limited mitochondrial permeability
382 and redox balance may restrict neomycin's effective access.

383 Based on our findings, we re-evaluated several hypotheses for this striking *in vivo / in*
384 *vitro* divergence. While the cellular redox state was a possible candidate given prior
385 research on neomycin toxicity[45,46], our translation assays showed that the reducing
386 agents TCEP or GSH had only a minimal effect on neomycin's inhibitory action (**Fig. 4**,
387 **Supplementary Fig. 8**). This suggests that the redox environment is not the primary
388 mechanism responsible for neomycin's lack of binding at the key h44 site. Instead, we
389 propose that other robust cellular mechanisms, such as drug efflux, are critically involved.
390 This is further supported by the observed restricted engagement of neomycin on the
391 ribosomes at higher neomycin concentrations (**Supplementary Tables 4-5**). Beyond
392 direct ribosomal inhibition, other potential toxicity mechanisms exist, as exemplified by a
393 recent finding that neomycin induces toxicity by mediating PGC-1α imbalance of
394 mitochondria-lipid droplet homeostasis[30].

395 Expanding on these insights, our observations reveal that neomycin binding is highly
396 sensitive to the ribosomal state, aligning with the known mechanism by which 4,5-linked
397 aminoglycosides stabilize the non-rotated state and inhibit translocation[24,27]. Furthermore,
398 while the binding of neomycin to mitoribosomes and cytosolic ribosomes differs overall,
399 the fundamental contact modules of neomycin remain conserved. To investigate this in
400 detail, we quantified the interacting frequency of each neomycin atom across previously
401 reported bacterial ribosome structures and human ribosome structures (mitoribosome
402 and cytosolic ribosome) determined in our study. Our analysis revealed that, consistent
403 with prior bacterial studies, rings I and II of neomycin are the most frequently utilized
404 moieties for ribosomal interaction[24,27], playing a crucial role in neomycin's binding

405 (**Supplementary Fig. 9g**). Specifically, these two -NH_2 groups from ring II (2-DOS ring,
406 the core of aminoglycosides) exhibit the highest frequency of interactions across all three
407 ribosome types, closely followed by the -OH and 6'-NH_2 groups from ring I
408 (**Supplementary Fig. 9g**). The strong binding capabilities of these amino groups stem
409 from their ability to form hydrogen bonds with phosphate oxygen atoms within the
410 ribosome's rRNA backbone or with nucleotide hydroxyl groups. Furthermore, their typical
411 positive charge enables robust electrostatic interactions with the negatively charged
412 phosphate backbone of the ribosome.

413 Collectively, our study demonstrates that neomycin-ribosome interactions are not static
414 but highly sensitive to various factors, such as the ribosomal state and cellular
415 environment, indicating an additional level of complexity in the ribosome-antibiotic binding
416 studies. Moreover, our findings challenge the prevailing assumption that mitochondrial
417 translation inhibition is the primary cause of neomycin toxicity, as neomycin was notably
418 absent on native mitoribosomes *in vivo*. Instead, toxicity may involve metabolic
419 disturbances or drug accumulation under pathological conditions. The resilience of
420 mitoribosomes to neomycin may also arise from an adaptive cellular response, inherent
421 insensitivity to certain threshold levels, or a limited import into mitochondria. However, the
422 specific mechanistic processes essential for neomycin binding warrant further
423 investigation. In the future, the structural studies of native samples will help to better
424 understand the related pathological dysfunctions.

425

426 **Methods**

427 **Cell lines and cell culture**

428 HEK293T cells were cultured at 37 °C and 5% CO_2 in Dulbecco's Modified Eagle's
429 Medium (DMEM, Gibco, C11995500BT) supplemented with 10% fetal bovine serum (FBS,
430 Excell Bio, FSP500). HEK293F cells were cultured in SMM 293-TII expression medium
431 (Sino Bio, M293TII) in shake flasks at 37 °C, 5% CO_2 and 110 rpm.

432

433 **Plasmid construction and generation of stable cell lines**

434 Clonal stable cell lines expressing NanoLuciferase (NLuc) or cystic fibrosis
435 transmembrane conductance regulator (CFTR) were generated as previously described[47].
436 The NLuc expression construct was generated by PCR amplification of NLuc-Flag
437 fragments, subsequently assembled into a linearized vector (originally derived from Jamie
438 H. D. Cate's laboratory) via Gibson Assembly. For the *CFTR* plasmid, *CFTR-G542X*
439 *(UGA)* along with the G542X context (seven codons upstream and downstream) was
440 fused to NLuc. This recombinant fragment was cloned into the same laboratory-derived
441 backbone vector using Gibson Assembly. The CFTR-G542X mutant was created through
442 site-directed mutagenesis of wild-type *CFTR* cDNA templates. The plasmid construct was
443 subsequently transfected into HEK293T cells and stable transfectants were selected
444 using 1 μg/ml puromycin for two weeks.

445

446 ***In vivo* translation assays**

447 The effect of neomycin on cytosolic translation was evaluated using the NLuc cell lines,
448 which were exposed to different concentrations of neomycin (0.5, 1, 2 and 3 mM) or
449 DMEM as a control. Luciferase activity was quantified after 1, 4, and 24 h using microplate
450 luminometer (BERTHOLD, Centro XS3 LB 960). To access the impact of the redox
451 environment on neomycin toxicity, 0.3 mM H_2O_2 was co-administered with varying
452 concentrations of neomycin (0.1, 1, and 3 mM) for 1 h. Additionally, to determine the
453 readthrough effect of neomycin, the CFTR cell lines were treated with different
454 concentrations of neomycin (0.5, 1, 2, and 3 mM) for 24 h and 48 h, respectively.

455

456 ***In vitro* transcription and translation assays**

457 The DNA template for *in vitro* transcription was PCR-amplified from plasmid pGM_EMCV-
458 NLuc using primers encoding T7 RNA polymerase promoter and poly-A tail sequences.
459 The *in vitro* transcription reaction was performed as previously described[47]. mRNA
460 transcripts were assessed for quality and size by gel electrophoresis, quantified
461 spectrophotometrically (Implen spectrophotometer, Nanophotometer NP80), diluted to 1
462 μg/μL, aliquoted, and preserved at -80 °C prior to *in vitro* translation reactions.

463 HEK293T cells were harvested at ~80% confluency and resuspended in ice-cold lysis
464 buffer (10 mM HEPES-KOH pH 7.5, 10 mM KOAc, 0.5 mM $Mg(OAc)_2$, 5 mM DTT) at a
465 1:1 (v/v) ratio. The HEK293T cell lysates and IVT reaction systems were prepared as
466 described previously[48,49]. Neomycin (MCE, HY-17624A) was introduced at different
467 concentrations as experimental variables in the reaction system at final concentrations of
468 1 μM, 5 μM, 10 μM, 15 μM, 25 μM, 30 μM, 40 μM, 50 μM and 100 μM. Reactions were
469 equilibrated at 30 °C for 25 min prior to luciferase activity measurement using a microplate
470 luminometer (BERTHOLD, Centro XS3 LB 960). Lysates and mRNA aliquots from
471 identical preparation lots were used for comparative assays within individual experimental
472 series to control batch variability.

473

474 **Cell counting kit-8 (CCK-8) cell growth assay**

475 The cytotoxicity of neomycin was measured in HEK293T cell lines using the CCK-8 assay.
476 Approximately 8000 cells per well were seeded in a 96-well plate in DMEM medium
477 supplemented with 10% FBS. After 24 h of adhesion, the cells were treated with different
478 concentrations of neomycin dilutions versus DMEM vehicle control. After 72 h of
479 incubation, culture medium was replaced with fresh DMEM medium supplemented with
480 CCK-8 (10% v/v reagent: medium ratio) for an additional 2 h of light-protected incubation.
481 Cellular viability was determined by measuring at 450 nm using a microplate reader. The
482 half-maximal inhibitory concentration (IC_{50}) for neomycin was calculated by fitting the
483 dose-response curve using GraphPad Prism software. All experiments were performed
484 in biological triplicates (n = 3).

485

486 **L-AHA labeling of nascent polypeptides**

487 L-AHA labeling of mitochondrial-encoded nascent polypeptides was performed as
488 described previously[39]. Briefly, the cells were treated with different concentrations of
489 neomycin and 50 μg/mL cycloheximide (CHX, MCE, HY-12320), which selectively inhibits
490 eukaryotic cytosolic ribosome activity by blocking translational elongation. Fluorescence
491 signals were analyzed using an Amersham Typhoon 5 (Cytiva).

492 For the cytosolic nascent polypeptide labeling, the procedure mirrored that used for
493 mitochondrial-encoded nascent polypeptides, with cells treated with 50 μg/mL CHX as a
494 positive control. Following the labeling, cells were harvested and resuspended in buffer
495 containing 60 mM Tris-HCl pH 8.0, 50 mM NaCl, 2 mM $MgCl_2$, 40 mM KCl, 5% glycerol,
496 0.1% NP-40 and 1× protease inhibitor and were subsequently homogenized on ice using
497 a glass dounce homogenizer. The resulting cell lysate was cleared by centrifugation at
498 15,000 ×*g* for 15 min at 4 °C, and the supernatant was transferred to new 1.5 mL tubes.
499 The click reaction and the following protein signal detection were performed as described
500 above. All experiments were performed in triplicate (n = 3 independent experiments).

501

502 **Isolation of mitochondria and purification of mitoribosomes**

503 Mitochondria isolation was performed as described previously[42]. A final volume of 1L
504 HEK293F cells at a density of 3×10^6 cells/ml was harvested, washed with Phosphate
505 Buffered Saline (PBS) buffer, and resuspended in 60mL mitochondrial isolation buffer (50
506 mM HEPES-KOH pH 7.5, 10 mM KCl, 1.5 mM $MgCl_2$, 1 mM EDTA, 1 mM EGTA, 1 mM
507 DTT, protease inhibitors). Cells were lysed by grinding in a glass dounce homogenizer
508 and lysate was clarified by centrifugation at 1000 ×*g* for 15 min, then 10,000 ×*g* for 15min
509 at 4°C to get the crude mitochondria in the pellet. The resulting pellet was resuspended
510 in 10 mL resuspension buffer (50 mM HEPES-KOH pH 7.5, 10 mM KCl, 1.5 mM $MgCl_2$,
511 1 mM EDTA, 1 mM EGTA, 1 mM DTT, 70 mM sucrose, 210 mM mannitol, and 1× protease
512 inhibitor). Genomic DNA was removed by adding of 100 U RNase-free DNase I and
513 centrifugation at 10,000 ×*g* for 15 min at 4 °C. The crude mitochondria were gently
514 resuspended in 1 mL buffer containing 20 mM HEPES-KOH pH 7.5, 1 mM EDTA, 250
515 mM sucrose and loaded onto sucrose gradients comprising 1.5 mL 60% (w/v), 4 mL 32%
516 (w/v), 1.5 mL 23% (w/v) and 1.5 mL 15% (w/v) sucrose solutions in 20 mM HEPES-KOH
517 pH 7.5, 1 mM EDTA. The gradients were centrifuged at 28,000 rpm for 1h at 4 °C using
518 an SW41Ti rotor (Beckman Coulter). The brown band containing mitochondria migrating
519 to the interface of 32% and 60% sucrose was collected.

520 The fresh isolated mitochondria were resuspended in lysis buffer (25 mM HEPES-KOH
521 pH 7.5, 100 mM KCl, 10 mM $Mg(OAc)_2$, 1.7% Triton X-100, 2 mM DTT, 1× protease

522 inhibitor) at a mitochondria-to-buffer ratio of 1:2 (v/v). The mixture was homogenized with
523 a glass dounce homogenizer. The lysate was cleared by centrifugation at 30,000 ×*g* for
524 20 min at 4 °C. The supernatant was then loaded onto the top of sucrose cushion (1 M
525 sucrose in 20 mM HEPES-KOH pH 7.5, 100 mM KCl, 20 mM $Mg(OAc)_2$, 1% TX-100, 2
526 mM DTT) and centrifuged at 339,200 ×*g* for 45 minutes at 4°C using an MLA130 rotor
527 (Beckman Coulter). The pellet was rinsed and resuspended in Grid buffer (20 mM
528 HEPES-KOH pH 7.5, 100 mM KCl, 10 mM $Mg(OAc)_2$, 0.02% DDM, 1 mM DTT).
529 Mitoribosomes (280 nM) were incubated with 50 μM neomycin (~178-fold excess) for
530 30 min at 4 °C prior to the cryo-EM sample preparation (molar ratio of ribosome to
531 neomycin around 1:170).
532

533 **Human cytosolic ribosome purification**

534 The human cytosolic ribosome was isolated using a modified protocol adapted from a
535 previously published paper[50]. HEK293T cells were harvested at ~80% confluency,
536 centrifuged at 1000 ×*g* for 10 minutes at 4 °C, and washed twice with ice-cold PBS. The
537 cell pellet was resuspended in an equal volume of lysis buffer (10 mM HEPES-KOH pH
538 7.5, 10 mM KOAc, 0.5 mM $Mg(OAc)_2$, 5 mM DTT). Following 20 min incubation on ice,
539 the resuspended cells were mechanically lysed by grinding in a glass homogenizer.
540 Lysates were centrifuged at 1,000 ×*g* for 10 min to remove cell debris, and cleared by
541 centrifugation at 10,000 ×*g* for 15 min at 4 °C. The supernatant was then loaded onto a
542 sucrose cushion (10 mM HEPES-KOH pH 7.5, 50 mM KCl, 5mM $Mg(OAc)_2$, 0.02% DDM,
543 1 mM DTT, 1M sucrose) and centrifuged at 603,000 ×*g* for 45 min at 4 °C in an MLA130
544 Rotor (Beckman Coulter). The pellets obtained were washed and sequentially
545 resuspended in Grid buffer (20 mM HEPES-KOH pH 7.5, 50 mM KCl, 5 mM $Mg(OAc)_2$,
546 0.02% DDM) and measured using an Implen spectrophotometer. Cytosolic ribosomes
547 (294 nM) were incubated with 50 μM neomycin (~170-fold excess) for 30 min at 4 °C prior
548 to the cryo-EM sample preparation (molar ratio of ribosome to neomycin around 1:170).
549

550 **Isolation of mitoribosome and cytosolic ribosome from neomycin treated cells**

551 HEK293F was scaled up sequentially, by inoculating at 1×10^6 cells/mL and subsequently
552 splitting at a cell density of 3.0×10^6 cells/mL until achieving 300 mL final culture volume.

553 Neomycin was added to HEK293F cells to a final concentration of 1 mM for 1 hour prior
554 to utilization. Native human mitoribosomes purification was performed as described for
555 the “Isolation of mitochondria and purification of mitoribosomes” part. And no extra
556 neomycin was added during the purification. The same batch of cells were used for
557 cytosolic ribosome isolation to make strict comparison, meaning we have native
558 mitoribosomes and cytosolic ribosomes from the same cells. After cells harvest and lysis,
559 the supernatant was applied for cytosolic ribosome isolation and the pellet was for crude
560 mitochondria isolation. The protocol for purification of cytosolic ribosomes is the same as
561 described in “Human cytosolic ribosome purification”. For the high concentration
562 neomycin treated cells, we treated the cells with 3 mM neomycin for 3 h and then
563 conducted the cytosolic ribosomes isolation as described.
564

565 **Cryo-EM grids preparation**

566 The concentrations of the mitoribosomes and cytosolic ribosomes used for cryo-EM grid
567 preparation were 280 nM and 160 nM, respectively. Approximately, 3.2 µL aliquots were
568 applied to a plasma-cleaned holey carbon grid (R1.2/1.3, 300 mesh, Quantfoil) for 1 min,
569 on which a homemade continuous carbon film was precoated. Grids were blotted for 2.5 s
570 under 100% humidity at 4 °C and plunge-frozen in liquid ethane using Vitrobot Mark IV
571 (Thermo Fisher Scientific).
572

573 **Cryo-EM data collection and processing**

574 Cryo-EM micrographs of all samples were collected on a Titan Krios transmission electron
575 microscope (Thermo Fisher Scientific) operated at 300 kV using a slit width of 20 eV on
576 a GIF quantum energy filter (Gatan). The micrographs were recorded using a Falcon 4i
577 direct electron detector at a pixel size of 0.81 Å. A total electron dose of 50 electrons per
578 $Å^2$ was fractionated over 40 frames with a total exposure time of 5.9 s. Data were acquired
579 using EPU software[50] with a defocus ranging from 1.0 to 2.0 µm.

580 All datasets were processed using cryoSPARC v.4.2.1[51]. The movie stacks were first
581 corrected for motion using the patch motion correction tool of cryoSPARC. Contrast
582 transfer function (CTF) parameters were estimated using the patch CTF estimation tool.
583 Manual curation was performed to exclude suboptimal micrographs. From the curated

584 micrographs, particles were initially identified through blob-based template-free picking,
585 followed by iterative template-based particle picking using averaging projections selected
586 from 2D classification. The extracted particles underwent multiple rounds of 2D
587 classification to remove non-ribosomal contaminants and ice artifacts. Particles were then
588 used for 3D auto-refinement yielding a map for further classification.

589 Focused 3D classification was carried out using a mask on the SSU to facilitate
590 conformational sorting, enabling separation of rotated versus non-rotated ribosome states.
591 Another round of focused 3D classification using a spherical mask on the tRNA binding
592 sites was performed, separating the particles into different tRNA binding states. H69 and
593 h44 are key binding sites of aminoglycoside antibiotics. Therefore, a spherical mask of
594 radius 23 Å was generated for H69 and h44, respectively, for 3D classification to improve
595 the local resolution. Masks with smoothed edges were generated with the
596 "relion_mask_create" tool in RELION4.0.0[52]. After one round of CTF refinement, particles
597 of each class were further processed by focused refinements with different masks applied.
598 All reported map resolutions were determined by the FSC = 0.143 cutoff criterion.

599

600 **Model building and refinement**

601 In general, the structures of cytosolic ribosomes (PDB: 8QOI[53]) and mitoribosome (PDB:
602 7QI5 and 7QI6[15]) were used for rigid body docking into the cryo-EM density map using
603 UCSF ChimeraX v1.8[54]. The docked coordinates were realigned to match map orientation
604 and saved as models for manual building and adjustment in Coot v0.9.8.1[55]. The
605 neomycin ligand was fetched from the Coot ligand library using the three-letter code: NMY
606 and manually positioned according to the density maps. Conformational changes induced
607 by neomycin binding were also manually adjusted. And the unknown continuous density
608 was analyzed using CryFold[56] to predict the sequence and three-dimensional structure,
609 which was subsequently added into the model. Final models were further subjected to
610 refinement with Phenix.real_space_refine v1.13_2998[57,58]. The figures were prepared
611 with ChimeraX v1.8[54]. Figures were compiled using Adobe Illustrator.

612 **Computational methods**

613 mtSSU molecular dynamics (MD) simulations were performed using the AMBER package.
614 The system comprised ribosomal proteins, rRNA, and three neomycin molecules (Neo1,
615 Neo2, Neo3) solvated in an orthorhombic TIP3P water box extending 12 Å beyond the
616 solute. The ff19SB force field was applied to proteins, OL3 to RNA, and GAFF2
617 parameters with AM1-BCC charges to ligands. After energy minimization and stepwise
618 heating, production runs were conducted at 90 K, 280 K, 290 K, 300 K, and 310 K under
619 NPT conditions using a 2-fs timestep with SHAKE constraints. Five independent 100-ns
620 replicates per temperature were acquired. Binding free energies were calculated via the
621 linear interaction energy method using the *cpptraj* module in Ambertools. And the MD of
622 the SSU of the cytosolic ribosome with three neomycin molecules (Neo1, Neo10, and
623 Neo11) were performed as described for the mtSSU.

624

625 **Neomycin Occupancy Estimation**

626 Neomycin occupancy was estimated for both the mitoribosomes and cytosolic ribosomes
627 using OccuPy (v0.1.9)[59], following the software's documentation for compositional
628 heterogeneity analysis. Briefly, we processed the input cryo-EM maps through a local
629 filtering approach to generate local resolution maps. These maps were subsequently
630 used to modify the original density maps by applying an amplification power and a final
631 output low-pass filter. The final neomycin occupancy was visualized by coloring the
632 original density maps according to the modified output maps in ChimeraX v1.8[54]. This
633 process effectively highlighted the regions of neomycin binding across both ribosome
634 types.

635

636 **Reporting summary**

637 Further information on research design is available in the Nature Research Reporting
638 Summary linked to this paper.

639

640 **Data availability**

641 The data that support the findings of this study are available from the corresponding
642 authors upon reasonable request. The cryo-EM maps have been deposited in the
643 Electron Microscopy Data Bank and the Protein Data Bank under the following accession
644 numbers: EMD-65426 and 9W80 (*in vitro* dataset, mitoribosomes in non-rotated state
645 with A/A P/P E/E-site tRNA), EMD-65433 and 9VXM (*in vitro* dataset, mitoribosomes in
646 non-rotated state with A/A P/P-site tRNA), EMD-65428 and 9W85 (*in vitro* dataset,
647 mitoribosome in partially rotated state with A/P P/E-site tRNA), EMD-65427 and 9W86 (*in*
648 *vitro* dataset, mitoribosome in partially rotated state with A/A P/P E/E-site tRNA), EMD-
649 65431 and 9W84 (*in vitro* dataset, mitoribosome in rotated state with A/P P/E-site tRNA),
650 EMD-65429 and 9W82 (*in vitro* dataset, mitoribosome in rotated); EMD-65419 and 9W7Z
651 (*in vitro* dataset, cytosolic ribosome in non-rotated state with P/P E/E-site tRNA), EMD-
652 65412 and 9W83 (*in vitro* dataset, cytosolic ribosome in partially rotated state with eEF2,
653 SERBP1 and E/E-site tRNA), EMD-65434 and 9VXN (*in vitro* dataset, cytosolic ribosome
654 in rotated state with A/P P/E-site tRNA), EMD-65411 (1 mM native dataset, cytosolic
655 ribosome in non-rotated state with P/P E/E-site tRNA), EMD-65413 (1 mM native dataset,
656 cytosolic ribosome in partially-rotated state with eEF2, SERBP1 and E/E-site tRNA),
657 EMD-65415 (1 mM native dataset, cytosolic ribosome in rotated state with A/P P/E-site
658 tRNA), EMD-65414 (1 mM native dataset, cytosolic ribosome in rotated state with A/A
659 P/E-site tRNA); EMD-65416 (3 mM native dataset, cytosolic ribosome in non-rotated state
660 with P/P E/E-site tRNA), EMD-65417 (3 mM native dataset, cytosolic ribosome in
661 partially-rotated state with eEF2, SERBP1 and E/E-site tRNA), EMD-65418 (3 mM native
662 dataset, cytosolic ribosome in rotated state with A/P P/E-site tRNA); EMD-65421 (1 mM
663 native dataset, mitoribosome in non-rotated state with P/P E/E-site tRNA), EMD-65422
664 (1 mM native dataset, mitoribosome in non-rotated state with A/A P/P E/E-site tRNA),
665 EMD-65423 (1 mM native dataset, mitoribosome in partially rotated state with A/A P/P-
666 site tRNA); EMD-65424 (native dataset, mitoribosome in partially rotated state with A/P
667 P/E-site tRNA), EMD-65425 (native dataset, mitoribosome in rotated state with P/E-site
668 tRNA), EMD-65420 (native dataset, LSU of the mitoribosome). Source data are provided
669 with this paper.

670

671 **Acknowledgements**

We thank Zhengkun Xie from the Center of Advanced Analysis & Gene Sequencing of Zhengzhou University for technical support, Jamie Doudna Cate and Jingdong Cheng for helpful discussions. This work was supported by grants from the National Natural Science Foundation of China (32171291 and 32371351 to W.L., 82302100 to M.W.), National Key Research and Development Program of China (2022YFA0807100 to W.L., 2023YFC2308900 to M.W.), Nature Science Foundation of Shandong Province (ZR2021QC002 to W.L.) the Shandong Excellent Young Scientists Fund Program (2022HWYQ-025), Taishan Scholars Program (tsqnz20221104), Cutting Edge Development Fund of Advanced Medical Research Institute (GYY2023QY01) and the Cheeloo Youth Program of Shandong University to W.L., European Research Council (805230) to A.A..

Contributions

X.Z., L.Z., C.J. and M.W. performed the sample preparation, acquired cryo-EM data, and carried out image processing and structure refinement. L.Z., C.J., W.M. and W.L. did the model building and structural analysis. X.Z., L.Z. and K.W. conducted biochemistry and cell-based experiments. X.H. performed the MD experiment. L.Z., W.L., C.J., W.M. and A.A. prepared the figures. W.L. and A.A. wrote the initial draft of the paper. All authors analyzed the data and edited the paper.

Competing interests

The authors declare no competing interests.

References

1. Kohanski, M. A., Dwyer, D. J. & Collins, J. J. How antibiotics kill bacteria: from targets to networks. *Nat. Rev. Microbiol.* **8**, 423–435 (2010).
2. Lin, J., Zhou, D., Steitz, T. A., Polikanov, Y. S. & Gagnon, M. G. Ribosome-targeting antibiotics: Modes of action, mechanisms of resistance, and implications for drug design. *Annu. Rev. Biochem.* **87**, 451–478 (2018).
3. Paternoga, H. *et al.* Structural conservation of antibiotic interaction with ribosomes. *Nat. Struct. Mol. Biol.* **30**, 1380–1392 (2023).

4. Wilson, D. N. Ribosome-targeting antibiotics and mechanisms of bacterial resistance. *Nat. Rev. Microbiol.* **12**, 35–48 (2014).
5. Becker, B. & Cooper, M. A. Aminoglycoside antibiotics in the 21st century. *ACS Chem. Biol.* **8**, 105–115 (2013).
6. Zaher, H. S. & Green, R. Fidelity at the molecular level: lessons from protein synthesis. *Cell* **136**, 746–762 (2009).
7. Recht, M. I., Douthwaite, S. & Puglisi, J. D. Basis for prokaryotic specificity of action of aminoglycoside antibiotics. *EMBO J.* **18**, 3133–3138 (1999).
8. Moazed, D. & Noller, H. F. Interaction of antibiotics with functional sites in 16S ribosomal RNA. *Nature* **327**, 389–394 (1987).
9. Prezant, T. R. *et al.* Mitochondrial ribosomal RNA mutation associated with both antibiotic-induced and non-syndromic deafness. *Nat. Genet.* **4**, 289–294 (1993).
10. Böttger, E. C., Springer, B., Prammananan, T., Kidan, Y. & Sander, P. Structural basis for selectivity and toxicity of ribosomal antibiotics. *EMBO Rep.* **2**, 318–323 (2001).
11. Hobbie, S. N. *et al.* Genetic analysis of interactions with eukaryotic rRNA identify the mitoribosome as target in aminoglycoside ototoxicity. *Proc. Natl. Acad. Sci. U. S. A.* **105**, 20888–20893 (2008).
12. Guan, M.-X. Mitochondrial 12S rRNA mutations associated with aminoglycoside ototoxicity. *Mitochondrion* **11**, 237–245 (2011).
13. Matt, T. *et al.* Dissociation of antibacterial activity and aminoglycoside ototoxicity in the 4-monosubstituted 2-deoxystreptamine apramycin. *Proc. Natl. Acad. Sci. U. S. A.* **109**, 10984–10989 (2012).
14. Amunts, A., Brown, A., Toots, J., Scheres, S. H. W. & Ramakrishnan, V. Ribosome. The structure of the human mitochondrial ribosome. *Science* **348**, 95–98 (2015).
15. Singh, V. *et al.* Mitoribosome structure with cofactors and modifications reveals mechanism of ligand binding and interactions with L1 stalk. *Nat. Commun.* **15**, 4272 (2024).
16. Fosso, M. Y., Li, Y. & Garneau-Tsodikova, S. New trends in aminoglycosides use. *Medchemcomm* **5**, 1075–1091 (2014).
17. Prokhorova, I. *et al.* Aminoglycoside interactions and impacts on the eukaryotic ribosome. *Proc. Natl. Acad. Sci. U. S. A.* **114**, E10899–E10908 (2017).
18. Palmer, E., Wilhelm, J. M. & Sherman, F. Phenotypic suppression of nonsense mutants in yeast by aminoglycoside antibiotics. *Nature* **277**, 148–150 (1979).
19. Manuvakhova, M., Keeling, K. & Bedwell, D. M. Aminoglycoside antibiotics mediate context-dependent suppression of termination codons in a mammalian translation system. *RNA* **6**, 1044–1055 (2000).
20. Keeling, K. M., Xue, X., Gunn, G. & Bedwell, D. M. Therapeutics based on stop codon readthrough. *Annu. Rev. Genomics Hum. Genet.* **15**, 371–394 (2014).
21. Shalev, M. *et al.* Structural basis for selective targeting of leishmanial ribosomes: aminoglycoside derivatives as promising therapeutics. *Nucleic Acids Res.* **43**, 8601–8613 (2015).
22. Sabbavarapu, N. M. *et al.* Design of novel aminoglycoside derivatives with enhanced suppression of diseases-causing nonsense mutations. *ACS Med. Chem. Lett.* **7**, 418–423 (2016).
23. Benveniste, R. & Davies, J. Structure-activity relationships among the

749 aminoglycoside antibiotics: role of hydroxyl and amino groups. *Antimicrob. Agents*
750 *Chemother.* **4**, 402–409 (1973).
751 24. Wang, L. *et al.* Allosteric control of the ribosome by small-molecule antibiotics. *Nat.*
752 *Struct. Mol. Biol.* **19**, 957–963 (2012).
753 25. Wallis, M. G., von Ahsen, U., Schroeder, R. & Famulok, M. A novel RNA motif for
754 neomycin recognition. *Chem. Biol.* **2**, 543–552 (1995).
755 26. Borovinskaya, M. A. *et al.* Structural basis for aminoglycoside inhibition of bacterial
756 ribosome recycling. *Nat. Struct. Mol. Biol.* **14**, 727–732 (2007).
757 27. Wasserman, M. R. *et al.* Chemically related 4,5-linked aminoglycoside antibiotics
758 drive subunit rotation in opposite directions. *Nat. Commun.* **6**, 7896 (2015).
759 28. Fourmy, D., Recht, M. I., Blanchard, S. C. & Puglisi, J. D. Structure of the A site of
760 Escherichia coli 16S ribosomal RNA complexed with an aminoglycoside antibiotic.
761 *Science* **274**, 1367–1371 (1996).
762 29. Smolkin, B. *et al.* Towards catalytic antibiotics: Redesign of aminoglycosides to
763 catalytically disable bacterial ribosomes. *Chembiochem* **20**, 247–259 (2019).
764 30. Chen, B. *et al.* PGC-1α-mediated imbalance of mitochondria-lipid droplet
765 homeostasis in neomycin-induced ototoxicity and nephrotoxicity. *Acta Pharm. Sin. B.*
766 **14**, 4413–4430 (2024).
767 31. Itoh, Y. *et al.* Structure of the mitoribosomal small subunit with streptomycin reveals
768 Fe-S clusters and physiological molecules. *Elife* **11**, (2022).
769 32. Sighel, D. *et al.* Inhibition of mitochondrial translation suppresses glioblastoma stem
770 cell growth. *Cell Rep.* **35**, 109024 (2021).
771 33. Aibara, S., Andréll, J., Singh, V. & Amunts, A. Rapid isolation of the mitoribosome
772 from HEK cells. *J. Vis. Exp.* (2018) doi:10.3791/57877.
773 34. Carter, A. P. *et al.* Functional insights from the structure of the 30S ribosomal subunit
774 and its interactions with antibiotics. *Nature* **407**, 340–348 (2000).
775 35. Holm, M. *et al.* mRNA decoding in human is kinetically and structurally distinct from
776 bacteria. *Nature* **617**, 200–207 (2023).
777 36. Ogle, J. M. *et al.* Recognition of cognate transfer RNA by the 30S ribosomal subunit.
778 *Science* **292**, 897–902 (2001).
779 37. An, H., Ordureau, A., Körner, M., Paulo, J. A. & Harper, J. W. Systematic quantitative
780 analysis of ribosome inventory during nutrient stress. *Nature* **583**, 303–309 (2020).
781 38. Yousefi, R. *et al.* Monitoring mitochondrial translation in living cells. *EMBO Rep.* **22**,
782 e51635 (2021).
783 39. Li, X. *et al.* Structural basis for differential inhibition of eukaryotic ribosomes by
784 tigecycline. *Nat. Commun.* **15**, 5481 (2024).
785 40. Rosenberg, C. R., Fang, X. & Allison, K. R. Potentiating aminoglycoside antibiotics
786 to reduce their toxic side effects. *PLoS One* **15**, e0237948 (2020).
787 41. Le, T. A. *et al.* Aminoglycoside-related nephrotoxicity and ototoxicity in clinical
788 practice: A review of pathophysiological mechanism and treatment options. *Adv.*
789 *Ther.* **40**, 1357–1365 (2023).
790 42. Aibara, S., Singh, V., Modelska, A. & Amunts, A. Structural basis of mitochondrial
791 translation. *Elife* **9**, (2020).
792 43. Itoh, Y. *et al.* Mechanism of membrane-tethered mitochondrial protein synthesis.
793 *Science* **371**, 846–849 (2021).
794 44. Bock, L. V. & Grubmüller, H. Effects of cryo-EM cooling on structural ensembles. *Nat.*

Commun. **13**, 1709 (2022).
45. Hammill, T. L. & Campbell, K. C. Protection for medication-induced hearing loss: the state of the science. *Int. J. Audiol.* **57**, S67–S75 (2018).
46. Garetz, S. L., Altschuler, R. A. & Schacht, J. Attenuation of gentamicin ototoxicity by glutathione in the guinea pig in vivo. *Hear. Res.* **77**, 81–87 (1994).
47. Li, W., Chang, S. T.-L., Ward, F. R. & Cate, J. H. D. Selective inhibition of human translation termination by a drug-like compound. *Nat. Commun.* **11**, 4941 (2020).
48. Li, W. *et al.* Structural basis for selective stalling of human ribosome nascent chain complexes by a drug-like molecule. *Nat. Struct. Mol. Biol.* **26**, 501–509 (2019).
49. Lintner, N. G. *et al.* Selective stalling of human translation through small-molecule engagement of the ribosome nascent chain. *PLoS Biol.* **15**, e2001882 (2017).
50. Thompson, R. F., Iadanza, M. G., Hesketh, E. L., Rawson, S. & Ranson, N. A. Collection, pre-processing and on-the-fly analysis of data for high-resolution, single-particle cryo-electron microscopy. *Nat. Protoc.* **14**, 100–118 (2019).
51. Punjani, A., Rubinstein, J. L., Fleet, D. J. & Brubaker, M. A. cryoSPARC: algorithms for rapid unsupervised cryo-EM structure determination. *Nat. Methods* **14**, 290–296 (2017).
52. Kimanius, D., Dong, L., Sharov, G., Nakane, T. & Scheres, S. H. W. New tools for automated cryo-EM single-particle analysis in RELION-4.0. *Biochem. J.* **478**, 4169–4185 (2021).
53. Holvec, S. *et al.* The structure of the human 80S ribosome at 1.9 Å resolution reveals the molecular role of chemical modifications and ions in RNA. *Nat. Struct. Mol. Biol.* **31**, 1251–1264 (2024).
54. Goddard, T. D. *et al.* UCSF ChimeraX: Meeting modern challenges in visualization and analysis. *Protein Sci.* **27**, 14–25 (2018).
55. Emsley, P., Lohkamp, B., Scott, W. G. & Cowtan, K. Features and development of coot. *Acta Crystallogr. D Biol. Crystallogr.* **66**, 486–501 (2010).
56. Su, B., Huang, K., Peng, Z., Amunts, A. & Yang, J. Improved automated model building for cryo-EM maps using CryFold. *bioRxiv* (2024) doi:10.1101/2024.11.13.623164.
57. Afonine, P. V. *et al.* Real-space refinement in PHENIX for cryo-EM and crystallography. *Acta Crystallogr. D Struct. Biol.* **74**, 531–544 (2018).
58. Liebschner, D. *et al.* Macromolecular structure determination using X-rays, neutrons and electrons: recent developments in Phenix. *Acta Crystallogr. D Struct. Biol.* **75**, 861–877 (2019).
59. Forsberg, B. O., Shah, P. N. M. & Burt, A. A robust normalized local filter to estimate compositional heterogeneity directly from cryo-EM maps. *Nat. Commun.* **14**, 5802 (2023).